A Statistical Model of the Penetrating Arterioles and Venules in the Human Cerebral Cortex

Wahbi K. El-Bouri, Stephen J. Payne

Department of Engineering, Institute of Biomedical Engineering, University of Oxford, Parks Road, Oxford OX1 3PJ, UK

Short Title: Statistical Model of Penetrating Vessels

Grant Numbers: W.K. El-Bouri is funded by an EPSRC Doctoral Training Partnership studentship, grant reference EP/M50659X/1

Corresponding Address: Wahbi K. El-Bouri, Department of Engineering, Institute of Biomedical Engineering, University of Oxford, Parks Road, Oxford OX1 3PJ, UK

Keywords: Microcirculation, Murray's law, microvasculature, cerebral blood flow, vascular resistance

0. ABSTRACT

Objective

Models of the cerebral microvasculature are required at many different scales in order to understand the effects of microvascular topology on CBF. There are, however, no data-driven models at the arteriolar/venular scale. In this paper we develop a data-driven algorithm based on available data to generate statistically accurate penetrating arterioles and venules.

Methods

A novel order-based density-filling algorithm is developed, based on statistical data including bifurcating angles, LDRs, and area-ratios. Three thousand simulations are presented, and the results validated against morphological data. These are combined with a previous capillary network in order to calculate full vascular network parameters.

Results

Statistically accurate penetrating trees were successfully generated. All properties provided a good fit to experimental data. The *k* exponent had a median of 2.5 and an interquartile range of 1.75 – 3.7. CBF showed a standard deviation ranging from ±18% to ±34% of the mean, depending on the penetrating vessel diameter.

Conclusions

Small CBF variations indicate that the topology of the penetrating vessels plays only a small part in the large regional variations of CBF seen in the brain. These results open up the possibility of efficient oxygen and blood flow simulations at MRI voxel scales which can be directly validated against MRI data.

List of Abbreviations

LDR – Length-to-diameter ratio

CBF – Cerebral blood flow

BOLD – Blood oxygen level dependent

fMRI – Functional magnetic resonance imaging

IQR – Interquartile range

OEF – Oxygen extraction fraction

MTT – Mean transit time

1. Introduction

The brain's energy use, relative to its mass, is extremely high. Whilst on average the brain takes up just 2% of the mass of an adult human, it consumes 20% of the oxygen supply of the whole body [6]. This makes it particularly susceptible to damage and death when there are significant reductions in blood supply. The microvascular architecture is recognized as being key to the perfusion rate and the delivery of oxygen to the surrounding tissue [3,18,30]. Changes in the cerebral microvasculature topology have been linked to Alzheimer's disease and vascular dementia [15,23], vascular occlusions [25], and brain tumours [2,14].

However, little is known about the link between the microvascular topology and global scale blood and oxygen perfusion in the cortex. Imaging techniques, such as perfusion MRI, have spatial resolutions that are much larger than the microvasculature and hence are unable to easily discern the link between the microvasculature and global perfusion. Functional magnetic resonance imaging (fMRI) uses the blood oxygen level dependent (BOLD) technique as a surrogate signal to indicate neuronal activity. Its usefulness, however, "depends on an understanding of neurovascular coupling and the underlying vascular architecture" [4]. For example, Gagnon et al. recently attempted to quantify this link using two-photon microscopy on mice [11]. However, in order to better understand the interplay between the micro- and macro-scale we need mathematical models based on experimental data of the cerebral microvasculature. This will allow us to generate and analyse many different models and configurations of the cerebral vasculature. These statistical models, informed by one-off casts and animal experiments, can then be used in conjunction with these methods to help us better understand blood flow in the microvasculature, and simulate blood flow in a way that is not restricted to particular experimental conditions.

A wealth of data has recently become available on the architecture of the microvasculature in the human cortex. A series of studies by Duvernoy, Cassot, Lauwers, and Lorthois have produced statistical data on the structure and connectivity of the cerebral microvasculature, from the “tree-like” penetrating arterioles and venules that branch off the surface pial vessels, down to the “mesh-like” capillary networks that fill the grey matter [3-5,18,21]. Distinctions are made between the bifurcating arterioles and venules, and the highly connected capillary network. Bifurcating angles, area ratios, length-to-diameter ratios (LDR), vessel densities, and lengths are among the variables quantified in the data sets analysed, affording the opportunity to build statistically accurate microvascular models of the cortex.

A statistically accurate capillary model based on this data has already been established by Su et al. [32]. This model, however, modelled capillaries discretely, and so generating voxel size models of the capillary network (order of mm^3) proved computationally very expensive. As a result, El-Bouri and Payne [9] used multi-scale methods to homogenize the network and to convert it into a continuum based problem where the permeability of the capillary network is used to generate large voxel size models. A standard MRI voxel will, however, contain both capillaries and penetrating vessels. Therefore, a statistical model of the penetrating arterioles and venules is required in order to couple it with the capillary network in a given voxel. This would then give a representative model of the microvasculature in a typical MRI voxel, allowing us to explore the link between the microvasculature and perfusion measurements. This will also allow us to look at the relationship between flow and metabolism in more detail.

In previous studies, Lorthois et al. [20] used image segmentation to reconstruct the arteriole, venule, and capillary networks of a given region of the cortex. Guibert et al. [12] also used image segmentation to reconstruct a region of the microvasculature for the primate cortex. Although these reconstructed networks are useful, they are specific to only the region of the microvasculature that has been simulated and hence are neither generalizable nor scalable.

Karch et al. [17] used constrained constructive optimization combined with staged growth to generate arterial model trees. This framework works to minimise the intravascular volume of the tree whilst “optimizing the geometric location and topological site of each new connection” [17]. This method was also used by Linninger et al. [19] to generate penetrating arterioles and venules. Although choosing to minimise intravascular volume is reasonable, it is probably not the only principle at work [17], and recent analysis of human arterioles and venules has shown that the *k* value in Murray’s law can vary by 3 orders of magnitude [5]. Additionally, none of these models use the wealth of statistical data now available to construct their models, relying instead on a volume minimisation assumption; they are thus not data-driven models.

Supplementary data in [4] give statistical means, medians, and standard deviations of the area ratios and angles at bifurcations in the arterioles and venules analysed. These are listed by order of the vessel starting at order 4 – being the largest diameter vessels – to order 0 being the terminal vessels. As well as these, vessel densities are given, along with LDR distributions by order [21]. These distributions can be used to generate statistically accurate penetrating arterioles and venules in the human cortex. Using this data to construct these vessels therefore removes the need for any assumptions to be made regarding the minimisation of tree volume or form of the tree.

This work thus introduces a data-driven statistical 3-dimensional model of the penetrating arterioles and venules based on available morphological data, removing the need for any assumptions as used in previous models. A novel order-based density-filling algorithm is developed which generates statistically accurate arteriolar and venular penetrating trees. Three thousand simulations are run and the variables of interest are validated against penetrating vessel morphological parameters found in the literature. The penetrating vessels are then combined with the capillary network already available [32] and the total network parameters are validated against morphological values. The *k* exponent of Murray’s Law is calculated and

compared to the theoretical value. The vascular resistance of the penetrating trees is calculated to give a first order approximation to the CBF and to assess the variability of the CBF with the variations in topology modelled by the algorithm.

2. Materials and Methods

2.1. Morphological parameters

The data collation of the morphological parameters used in the model is split into two parts. The first part deals with parameters required to model the penetrating arteriolar or venular trunk. The second part concerns the parameters used to model the branching vessels that bifurcate from the main trunk.

2.1.1. Penetrating Arterioles/Venules

Penetrating arterioles and venules are randomly spaced at the pial surface and show conspicuous large arteriole and venular columns orthogonal to the cortical surface [25]. This observation suggests that penetrating vessels can be modelled individually and the various columns combined to form a volume of the cortex. Cuboid voxels are chosen here in which to model the individual trees. The surface area density of the penetrating vessels ranges from 8.44 – 15 /mm^2 [31] with approximately 2/3 of these vessels being arterioles and 1/3 venules [4,12]. As such, a surface area density of 12 vessels/mm^2 was chosen, in the ratio 8 arterioles to 4 venules. Assuming a square surface area at which the penetrating vessel enters the grey matter, this fixes the lengths of the square for the arterioles and venules. A square surface is chosen here as the penetrating trees are collated to form a realistic cuboidal voxel later on.

Most penetrating arterioles and venules penetrate to the middle of the cortex (although some penetrate all the way to the white matter) [8]. The depth of the cortex is approximately 2.5mm

[8], hence the depth of the cube was chosen here to be 1.25mm. Therefore an arteriole model will have dimensions of 0.35x0.35x1.25mm, and a venule model will be 0.5x0.5x1.25mm. Eight arterioles along with four venules embedded in a capillary bed running the depth of the cortex will have dimensions of 1x1x2.5mm, the same dimensions of a typical MRI voxel.

The most numerous penetrating arterioles range in diameter from 15 – 40 μm, with larger diameter vessels reaching 240 μm [8]. All arterioles of diameter 50 μm or less penetrate the cortex surface, with the largest diameter arterioles penetrating through to the white matter. Most of these penetrating arterioles have a diameter of approximately 40 μm [8]. The diameters remain approximately constant throughout the cortex, although some do have significant taper [25]. As a result, the diameter of the penetrating arterioles was chosen here to be 40 μm with the diameter remaining constant throughout the depth of the cube. Similarly, for the venules, a diameter of 110 μm was chosen, in keeping with experimental observation [8].

Finally, an initial order must be assigned to the penetrating trunk, as the parameters used in the construction of the artificial trees are order-based. The order system used here is the diameter-defined Strahler taxonomy [16] with the highest orders being assigned to the penetrating trunk and order 0 being terminal vessels. Cassot et al. [3] identified between 3 – 5 orders of arterioles before the capillary bed (where a capillary is defined as a vessel with a diameter less than 10 μm). As a result, the penetrating trunk is given an initial order of 4, which is changed if the final tree density is not within 5% of the morphological value. The variable values used for the construction of the penetrating trunks, along with their justification, are given in Table 1.

2.1.2. Branching Vessels

A wealth of data has recently become available on the geometric properties of penetrating arterioles and venules in the cortex [4]. This provides an opportunity to generate statistically and geometrically accurate penetrating arterioles and venules, similar to the statistical model already

in place for the capillary network in the cortex [9,32], without having to make any assumptions about the form of the branching.

Area-ratios, LDRs, and bifurcation angle distributions are all available in [21] and the supplementary material of [4]. The data are recorded by order of vessel, as well as for the total network of vessels in the cortex, making it straightforward to implement an order-based algorithm and to compare the results to the overall network parameters. The LDR distribution was found to be lognormal [21] , but no data on the standard deviation and mean of each order were given (although the median at each order was given). As a result, at each order, a mean was chosen and the standard deviation was altered so that the total network LDR matched the experimental data. Normal distributions were assumed at each order.

Area ratios were given at a bifurcation between the parent branch and large daughter branch (A01), the parent and the small daughter (A02), and the large daughter and small daughter (A12). The distributions were all lognormal with given mean, median, and standard deviation [4]. Similarly, the bifurcation angles were given between the various branches (α01, α02, α12). These were found to be approximately normally distributed with a given mean and standard deviation at each order.

2.1.3. Vessel Density

The algorithm developed here terminates when the appropriate vessel density has been reached for a given volume of the cortex. Cassot et al. found that in 28.6 mm^3 there were 11014 arteriolar segments and 8042 venular segments (with a ratio of 2:1 arteriolar arborisations to venular arborisations) [4]. Based on these values the vessel density required for the arterioles is 385.1 /mm^3 and for the venules is 281.2 /mm^3 (indicating that venules have more vessels per individual tree). These density values are used here to generate appropriate arteriolar and venular networks.

2.2. Algorithm

The novel order-based density-filling algorithm presented here produces statistically accurate columns of arteriolar and venular trees. The steps taken to produce these penetrating vessels are shown in the flowchart in Fig.1.

The length, diameter, order, and dimensions of the column are input to generate the initial trunk of the penetrating arteriole. The trunk is then randomly seeded with nodes following the probability density function of primary branches given in Blinder et al. [1]. The first bifurcation generated from these nodes will always be the small daughter. The order of this branch is found by sampling from the morphological probability distribution of the connectivity of varying orders of vessel given by Cassot et al. [4]. The LDR, area ratio, and bifurcation angle distributions for the small daughter branch are next used to find the length, radius, and angles of the first bifurcation, determining the position of the end node of that branch. The primary branches are oriented randomly about the penetrating trunk.

For the next bifurcation, again the orders of the daughter vessels are found by sampling from the morphological probability distributions. Values of radius and length for both the large daughter and small daughter are found and all 3 bifurcation angles are sampled from the normal distributions [4]. As a result, a constraint is imposed so that the sum of the three angles is always less than 2π (as the solid angle must be less than 2π). The radii, lengths, and bifurcation angles then uniquely determine the end nodes of the vessels. For arterioles, a twist about the parent branch of 90° is imposed to mimic the characteristic shape observed for arterioles. For venules, a random twist is imposed emulating their more lateral branching [8]. This branching is repeated until 4 orders of bifurcation have been reached, or all the terminal vessels are of order 0.

At this stage, the diameter-defined Strahler algorithm is used to calculate the mean and standard deviation of the diameters at each order. The vessels are then reassigned orders based on which order their diameter falls into. The density of the vessels is also calculated. Then three filters are used to ensure that the density is morphologically accurate. If a vessel is order 0 and has daughter branches, all the daughter branches are deleted. This filter is always used as an order 0 vessel must be terminal. Depending on whether the vessel density is too small or too large, two other filters are implemented. If the vessel density is too small, order 0 vessels are added to non-order 0 terminal vessels. If the density is too large, vessels are deleted starting with the smallest diameter vessels. Once a morphologically accurate density is finally reached the algorithm is terminated.

2.3. Vascular Resistance

The total vascular resistance of a penetrating tree is calculated and used to calculate blood perfusion as a first order approximation. Poiseuille flow is assumed in each vessel from which the resistance of the vessel can be found

$$\Delta P = RQ \tag{A.1}$$

$$R = \frac{8\mu(r)L}{\pi r^4} \tag{A.2}$$

where ΔP is the pressure drop in the vessel, Q is the flowrate, R is the resistance of the vessel, L is the length of the vessel, r is the radius of the vessel, and $\mu(r)$ is the apparent viscosity of the blood, which is dependent on the radius due to the Fahraeus-Lindqvist effect [10]. The apparent in-vivo viscosity can be calculated using the following relationship describing the variation of μ_{vivo} as a function of vessel diameter D (in micrometers) and discharge hematocrit H_{ct} (which is set here to be 0.45) [29].

$$\mu_{vitro} = \mu_p \left[1 + (\eta_{0.45} - 1)\frac{(1 - H_{ct})^{C_D} - 1}{(1 - 0.45)^{C_D} - 1}\right] \quad \text{(A.3)}$$

$$\eta_{0.45} = 220e^{-1.3D} + 3.2 - 2.44e^{-0.06D^{0.645}} \quad \text{(A.4)}$$

$$C_D = (0.8 + e^{-0.075D})\left(-1 + \frac{1}{1 + 10^{-11}.D^{12}}\right) + \frac{1}{1 + 10^{-11}.D^{12}} \quad \text{(A.5)}$$

$$\mu_{vivo} = \mu_{vitro}.\left(\frac{D}{D_{eff}}\right)^4 \quad \text{(A.6)}$$

μ_p is the viscosity of blood plasma (1.2 mPa s), μ_{vitro} is the in-vitro blood viscosity, and $\eta_{0.45}$ is the relative apparent viscosity of blood for a discharge hematocrit of 0.45. D_{eff} is the effective diameter of the blood vessel that takes into account the thickness of the endothelial surface layer and is derived using correlations detailed in Pries and Secomb [29].

Using equations A.2 – A.6 the resistance of any given vessel can be calculated. For a given tree, the resistances at bifurcations are calculated in parallel and added to the parent vessel resistance. This is repeated until a given tree has one resistance, R_{total}. It is assumed here for simplicity that all the terminal vessels exit to one pressure P_{out}. For arterioles the pressure drop across the penetrating arteriole (ΔP) is set to be 35 mmHg, and for venules the pressure drop is set to be 15 mmHg [34]. Using the pressure drop and the total resistance, the flow rate Q through the tree can be calculated using equation A.1 and from that the CBF using the following equation

$$CBF = \frac{Q \, x \, 1x10^6 \, x \, 60 \, x \, 100}{V \, x \, \rho} \quad \text{(A.7)}$$

where V is the volume of tissue the tree feeds, ρ is the cerebral tissue density (0.96 g cm^{-3}) [7,22], $1x10^6$ converts m^3 to mL, and 60 and 100 convert seconds to mins and g to 100g respectively. The volume of tissue fed by a given tree is unknown in this model. As a result it is chosen to be the cuboid volume that each arteriole/venule is generated in (the cuboid having a depth of 1.25mm). This of course may not be the region of influence of the penetrating vessel, but as we are only interested in the variation of the CBF with varying topology, this will not have an effect on our analysis.

2.4. Validation

Arterioles and venules are simulated over 1500 runs each. The algorithm uses statistics given at each order of vessel. Therefore the bifurcation area ratios, bifurcation angles, and LDRs can be calculated and compared against experimental data. As well as this, the arteriole/venule trees can be combined with a statistically accurate capillary network in order to calculate total network statistics such as total length, mean segment length, and vascular volume.

3. Results

Examples of random arteriolar trees generated using the algorithm outlined are shown in Fig. 2. They show clearly the variability in the shape and density of the penetrating vessels that the algorithm introduces due to its use of sampling from statistical data. The blood vessels were assumed to be straight thin-walled cylinders, hence the slightly artificial look of the penetrating trees in Fig. 2.

Three thousand simulations were run here in total, 1500 arterioles and 1500 venules. The results were then analysed and compared to morphological measurements.

3.1. LDR, Area Ratios & Bifurcation Angles

Histograms of the generated values of LDR, area ratios, and bifurcation angles for all the bifurcations in the 3000 simulations are given in Fig. 3, along with the approximate morphological distributions calculated by Lorthois et al. and Cassot et al. [4,21]. Note that, for a given bifurcation, A0 refers to the cross-sectional area of the parent vessel, A1 the cross-sectional area of the large daughter vessel, and A2 the cross-sectional area of the smaller daughter vessel. Similarly, α_{01} is the angle between the parent and large daughter, α_{02} is the angle between the parent and smaller daughter vessel, α_{12} is the angle between the two daughter vessels, and the asymmetry is the difference between α_{01} and α_{02}. The mean and standard deviations of the distributions fitted to the simulations presented here can be found in Table 2, along with the morphologically calculated parameters.

As can be seen by inspection there is, on the whole, a good fit to the morphological measurements. All the variables computed have a mean within the standard deviation of the experimental values (note that the mean vessel density values have no standard deviation as they are calculated from one 28.6 mm^3 sample). No hypothesis testing was undertaken due to the large number of vessels analysed and hence vanishingly small values of standard error involved.

The LDR and three area ratios were approximated as lognormal distributions by Cassot et al. [4], whilst the bifurcation angles were approximated as normal distributions. It should be noted that these are only approximations and that the real distributions from experimental

measurement are neither perfectly normal or perfectly lognormal. Hence exact agreement is not expected.

The bifurcation angle distributions from experimental data are also approximated as normal by Cassot et al. and hence extend beyond a value of 180º. However, no angle can be greater than 180º, as the algorithm always takes the smaller angle at a junction of two vessels; hence the histograms are cut off at this value whilst the experimental distribution extends beyond it.

3.2. Stem-Crown Analysis & Murray's Law

The normalized cumulative length (L/L_{max}) and volume (V/V_{max}) was computed for all the bifurcations generated by the model and these are shown in Fig. 4. L_{max} and V_{max} are the total cumulative length and the total cumulative volume respectively of a given penetrating tree. Each point in Fig. 4 corresponds to a stem-crown unit on a given tree, where a vessel segment is defined as a stem and the entire tree downstream of the stem is defined as the crown [33]. A power law relationship is found between the normalized length and normalized volume of the form:

$$\frac{V}{V_{max}} = \kappa \left(\frac{L}{L_{max}}\right)^{\gamma} \tag{A.8}$$

with parameter values γ = 1.239 ± 0.007 and κ = 1.17 ± 0.02. Cassot et al. [5] had previously found γ = 1.187 ± 0.003 and κ = 0.965 from morphological measurements. Both lines of best fit are plotted on a logarithmic graph in Fig. 4. As can be seen, there is very good agreement between the experimental and modelled results.

As well as this, the distribution of the exponent, *k*, of the generalized Murray's Law was calculated at every bifurcation (A.9).

$$d_o^k = d_1^k + d_2^k \quad \text{(A.9)}$$

where d_0 is the parent vessel diameter, d_1 is the large daughter vessel diameter, and d_2 is the small daughter vessel diameter. According to the minimum energy principle (and hence minimum volume principle) proposed by Murray [24], the *k* exponent is expected to have a value of 3. The median value of *k* found here was 2.5 with an interquartile range of 1.75 – 3.7. This is remarkably close to the value derived from physical principles by Murray. The spread of the *k* exponents over the different bifurcations is shown in Fig. 5. As can be seen, the *k* exponent varies from values below 1 all the way up to 25. There also appear to be peaks in the distribution at *k* values of 2, 3, 4, 6, 8, and 12. Despite investigation, the reason for these peaks is uncertain.

The spread in *k* shows that, although Murray's Law with a *k* exponent of 3 is a useful modelling rule, it is likely to over-simplify the complex geometry and interactions of the microvasculature. Therefore models that use a single *k* value of 3 to model the microvasculature should be used with caution.

3.3. Full Vascular Network

Su et al. [32] previously developed a statistically accurate capillary network of the human cortex, which was later homogenized and scaled-up by El-Bouri and Payne [9]. The geometric properties of that network can now be combined with the geometric properties of the arteriole/venule network developed here in order to analyse statistically the full vascular network, looking at parameters such as total length/mm^3, vascular surface/mm^3, and vascular volume. The results are summarised in Table 3. It should be noted that the vascular volume was calculated assuming that the capillary network extended the depth of the grey matter (2.5mm), but that the penetrating tree only extended halfway into the grey matter.

A specific morphological data set was used to compare against the model here. The data set in question had maximum vessel diameters of 25 μm [18]. Therefore in order to gain a meaningful comparison the algorithm was run with penetrating arterioles of diameter 25 μm. The resulting values of total length/mm^3, vascular surface/mm^3, vascular volume, volume/surface, and mean segment length are all remarkably close to the morphologically measured values, validating the volume filling algorithm. As a comparison, Linninger et al. [19] calculated a vascular surface/mm^3 of 13.60 mm^2/mm^3 and a vascular volume fraction of 2.49% using a volume minimisation algorithm for the arterioles/venules, which are also in good agreement with the morphological parameters.

We have thus shown that using order-based data extracted experimentally it is possible to reconstruct morphologically accurate penetrating arteriolar/venular trees, and full vascular networks in the cortex, without any assumptions. The algorithm is easily adaptable for different regions of the brain where the parameters may be different. As more data are obtained it will be possible to construct larger, morphologically accurate models of the blood vessels across different regions of the brain.

3.4. Vascular Resistance and CBF

The mean and standard deviation of the vascular resistance for the venule and arteriole trees, along with the calculated CBF is summarised in Table 4.

The 110 μm venule tree gives an accurate value for CBF of 46.0 mL min^{-1} 100g^{-1} which is close to the CBF values observed experimentally of 54.7 ± 6.1 mL min^{-1} 100g^{-1} [26]. The 40 μm and 25 μm arterioles, however, are one and two orders of magnitude smaller respectively than the morphologically value. From equation A.2 it can be seen that the vascular resistance is extremely sensitive to the radius as it is inversely proportional to the fourth power of the radii.

This leads to substantially larger resistances for smaller diameter vessels. When calculating CBF (A.7) the only variable is V, the volume of tissue the penetrating vessel perfuses. This depends on the assumption of the ratio of arterioles-to-venules and the number of penetrating vessels per mm^2. In this paper a 2:1 ratio of arterioles to venules has been assumed, but other papers assume a 3:1 ratio which would lead to larger values of arteriolar CBF [8,19]. As well as this, the region of influence of the penetrating vessel is unknown, making it difficult to accurately calculate the CBF using tree vascular resistances. Similarly, the assumption that a 25 μm arteriole will perfuse the same volume as a 40 μm arteriole is unlikely and also leads to the non-morphological values of CBF.

Of more interest, however, is the relative variability in CBF introduced by the statistical nature of the algorithm. Regardless of the penetrating vessel diameter, 50% of the CBF values remain within 20% of the mean CBF, indicating a tight distribution of the CBF. The interquartile range shows a slight asymmetry towards smaller CBF values. Therefore, it seems to be the case that the variations in CBF in various regions of the brain are only minimally affected by the varying topology of the vessels. The diameter of the penetrating vessel conversely has a much larger impact on the CBF, and hence oxygen delivery.

4. Discussion

In this paper, we have developed an algorithm to generate statistically accurate 3-dimensional models of the penetrating arterioles and venules based on data from a region of the cortex in the temporal lobe. The use of this data to generate penetrating arterioles/venules has meant that the assumptions of volume and energy minimisation previously used to model these trees [19] could be relaxed. This order-based density-filling algorithm was used to simulate 3000 penetrating trees from which morphological parameters of interest were calculated and validated against experimental data. A stem-crown analysis was conducted showing very close

agreement between the model and morphological measurements. Murray's *k* exponent was found to have a median of 2.5 with an IQR 1.75 – 3.7. This is an interesting result as no assumption was made with regards to the *k* exponent in the algorithm, yet it came out in very good agreement with the minimum energy *k* exponent of 3, indicating it is an emergent property of the model.

This penetrating vessel algorithm was then combined to a statistically accurate capillary generating algorithm [32] in order to calculate geometric parameters for the full vascular network. The resulting parameters of interest were all in very close agreement with the morphologically measured values (Table 3), validating the order-based density-filling algorithm developed here. Finally, the vascular resistance was calculated for the penetrating trees and from this, a first order approximation for CBF was calculated. The CBF was heavily affected by the radius of the penetrating vessel and the assumed volume of tissue the tree perfuses. However, the variability of the CBF with the quasi-random topology of the algorithm was < 34% of the mean CBF. This suggests that the variation of CBF in the brain is only nominally affected by the topology of the vessels, and is more likely to be affected by the varying vessel radii.

The only other 3-dimensional geometric construction algorithm for the cerebral microvasculature that we were able to find was that by Linninger et al. [19]. Minimum tree volume optimization was used to generate the penetrating arteriolar and venular trees which also provided a good match to the morphological data. This is based on the "minimum cost" concept proposed by Murray [24], a weighted minimum between the work needed to overcome the wall viscous stress and the building costs of the blood flow system. However, it is unlikely that minimising intravascular volume is the only principle at work in the construction of the penetrating vessels [17]. The model presented in this paper found a spread in the *k* exponent of less than 1 up to 25, with a median of 2.5. Therefore, a model built on this principle is likely to over-simplify the complex reality of the microvasculature. The *k* exponent is an emergent property of this model;

it was not specifically included as a property in the construction of the model. A model based on statistical data, like the one presented here, allows there to be a much more complex representation of the microvasculature without making assumptions with regards to minimising volume or energy. Therefore, a much more general model of the arterioles and venules can easily be adapted to differing regions of the brain when statistical data becomes available.

One limitation of this statistical model, however, is the lack of differentiation in the statistics between the arterioles and venules. The order-based data, given in the supplementary material of Cassot et al. [4], are not segregated by type of vessel (arteriole or venule). As a result, the penetrating trees generated use 'averaged' properties based on both the arterioles and venules. If vessel specific order-based data become available, however, it would be straightforward to adapt the distributions being sampled from accordingly and hence to generate more accurate arterioles and venules. Another limitation of the model is a lack of tortuosity in the vessels; they are approximated as straight thin-walled cylinders, as seen in Fig. 2. The curvature of penetrating arterioles and venules has been quantified by Lorthois et al. [21] and should be included in future works to generate more realistic networks, although it is anticipated that the effect on the blood flow through the vessels will be of second order due to the small curvature of individual vessels.

It should be noted that the algorithm developed in this paper is based on one set of experimental morphometric data, 28.6 mm^3 in size [4] (due to a lack of other accurate data on the human cerebral microvasculature). Therefore, the penetrating vessels generated in this paper characterize only a small region of the brain. It is very likely that different regions of the brain will have different statistics. However, once more information about the topology and geometry of the arterioles and venules in other areas of the human brain becomes available, the algorithm presented here is easily modifiable to generate realistic networks for individual regions.

The current algorithm is able to model voxel-size regions of penetrating vessels. The next step will be to couple the penetrating vessel network to the homogenized capillary network previously established [9] and to simulate blood flow. This would then be a mathematically rigorous data-driven multi-scale model of the blood flow in the cortex, where perturbation theory was used to generate statistically accurate homogenized capillary networks that can easily be scaled to large volumes, and the algorithm in this paper produced data-driven models of the penetrating vessels. The coupling of these two models will allow for the modelling of realistically sized MRI voxels from which cerebral blood flow and perfusion will be measured and compared to MRI data. This would help to establish the link between the microvasculature and the macro-scale flow in the cortex. Once the blood flow model has been established, it can then be coupled to oxygen transport models, from which mean transit time (MTT) and oxygen extraction fraction (OEF) can be calculated [27,28] and compared to experimental values. This will allow us to explore the interplay between topology and nutrient delivery and its robustness, as well as the effect of ischemic stroke on these values [13].

5. Perspectives

Through development of a novel data-driven algorithm to simulate the penetrating vessels in the microvasculature accurately, it is now possible to simulate cerebral blood flow at both the capillary and arteriole/venule scale in a way that is not restricted to particular experimental conditions. It is also possible to easily model the penetrating vessels in varying regions of the brain due to the data-driven aspect of the model as long as the statistical data are available. The coupling of the arteriole/venule and homogenized capillary models allows for MRI voxel scale simulations to be run efficiently which will allow us to better assess the impact of the microvascular architecture on blood and oxygen perfusion on the global scale.

REFERENCES

1. Blinder P, Tsai PS, Kaufhold JP, Knutsen PM, Suhl H, Kleinfeld D. The cortical angiome: an interconnected vascular network with noncolumnar patterns of blood flow. *Nat Neurosci* **16**: 889-897, 2013.

2. Bullitt E, Zeng D, Gerig G, Aylward S, Joshi S, Smith JK, Lin W, Ewend MG. Vessel tortuosity and brain tumor malignancy: a blinded study. *Academic radiology* **12**: 1232-1240, 2005.

3. Cassot F, Lauwers F, Fouard C, Prohaska S, Lauwers-Cances V. A novel three-dimensional computer-assisted method for a quantitative study of microvascular networks of the human cerebral cortex. *Microcirculation* **13**: 1-18, 2006.

4. Cassot F, Lauwers F, Lorthois S, Puwanarajah P, Cances-Lauwers V, Duvernoy H. Branching patterns for arterioles and venules of the human cerebral cortex. *Brain Res* **1313**: 62-78, 2010.

5. Cassot F, Lauwers F, Lorthois S, Puwanarajah P, Duvernoy H. Scaling laws for branching vessels of human cerebral cortex. *Microcirculation* **16**: 331-344, 332 p following 344, 2009.

6. Clarke DD, Sokoloff L. Circulation and Energy Metabolism of the Brain. In: *Basic Neurochemistry: Molecular, Cellular and Medical Aspects*, 5 edn, edited by Philadelphia: Lippincott-Raven, 1999, p. 645-680.

7. Dekaban AS, Sadowsky D. Changes in brain weights during the span of human life: Relation of brain weights to body heights and body weights. *Annals of Neurology* **4**: 345-356, 1978.

8. Duvernoy HM, Delon S, Vannson JL. Cortical blood vessels of the human brain. *Brain Research Bulletin* **7**: 519-579, 1981.

9. El-Bouri WK, Payne SJ. Multi-scale homogenization of blood flow in 3-dimensional human cerebral microvascular networks. *Journal of Theoretical Biology* **380**: 40-47, 2015.

10. Fahraeus R, Lindqvist T. The viscosity of the blood in narrow capillary tubes. *Amer J Physiol* **96**: 562-568, 1931.

11. Gagnon L, Sakadžić S, Lesage F, Musacchia JJ, Lefebvre J, Fang Q, Yücel MA, Evans KC, Mandeville ET, Cohen-Adad J, Polimeni JaR, Yaseen MA, Lo EH, Greve DN, Buxton RB, Dale AM, Devor A, Boas DA. Quantifying the Microvascular Origin of BOLD-fMRI from First Principles with Two-Photon Microscopy and an Oxygen-Sensitive Nanoprobe. *The Journal of Neuroscience* **35**: 3663-3675, 2015.

12. Guibert R, Fonta C, Plouraboue F. Cerebral blood flow modeling in primate cortex. *Journal of cerebral blood flow and metabolism : official journal of the International Society of Cerebral Blood Flow and Metabolism* **30**: 1860-1873, 2010.

13. Hayashi T, Watabe H, Kudomi N, Kim KM, Enmi J-I, Hayashida K, Iida H. A Theoretical Model of Oxygen Delivery and Metabolism for Physiologic Interpretation of Quantitative Cerebral Blood Flow and Metabolic Rate of Oxygen. *Journal of Cerebral Blood Flow & Metabolism* **23**: 1314-1323, 2003.

14. Jain RK. Normalization of tumor vasculature: an emerging concept in antiangiogenic therapy. *Science (New York, N.Y.)* **307**: 58-62, 2005.

15. Jellinger KA. The pathology of "vascular dementia": a critical update. *Journal of Alzheimer's disease : JAD* **14**: 107-123, 2008.

16. Jiang ZL, Kassab GS, Fung YC. Diameter-defined Strahler system and connectivity matrix of the pulmonary arterial tree. *Journal of applied physiology (Bethesda, Md. : 1985)* **76**: 882-892, 1994.

17. Karch R, Neumann F, Neumann M, Schreiner W. Staged growth of optimized arterial model trees. *Annals of biomedical engineering* **28**: 495-511, 2000.

18. Lauwers F, Cassot F, Lauwers-Cances V, Puwanarajah P, Duvernoy H. Morphometry of the human cerebral cortex microcirculation: general characteristics and space-related profiles. *Neuroimage* **39**: 936-948, 2008.

19. Linninger AA, Gould IG, Marinnan T, Hsu CY, Chojecki M, Alaraj A. Cerebral Microcirculation and Oxygen Tension in the Human Secondary Cortex. *Annals of Biomedical Engineering* **41**: 2264-2284, 2013.

20. Lorthois S, Cassot F, Lauwers F. Simulation study of brain blood flow regulation by intra-cortical arterioles in an anatomically accurate large human vascular network: Part I: methodology and baseline flow. *Neuroimage* **54**: 1031-1042, 2011.

21. Lorthois S, Lauwers F, Cassot F. Tortuosity and other vessel attributes for arterioles and venules of the human cerebral cortex. *Microvasc Res* **91**: 99-109, 2014.

22. Lüders E, Steinmetz H, Jäncke L. Brain size and grey matter volume in the healthy human brain. *NeuroReport* **13**: 2371-2374, 2002.

23. Meyer EP, Ulmann-Schuler A, Staufenbiel M, Krucker T. Altered morphology and 3D architecture of brain vasculature in a mouse model for Alzheimer's disease. *Proc Natl Acad Sci U S A* **105**: 3587-3592, 2008.

24. Murray CD. The Physiological Principle of Minimum Work: I. The Vascular System and the Cost of Blood Volume. *Proc Natl Acad Sci U S A* **12**: 207-214, 1926.

25. Nishimura N, Schaffer CB, Friedman B, Lyden PD, Kleinfeld D. Penetrating arterioles are a bottleneck in the perfusion of neocortex. *Proceedings of the National Academy of Sciences of the United States of America* **104**: 365-370, 2007.

26. Obrist WD, Thompson HK, King H, Wang HS. Determination of Regional Cerebral Blood Flow by Inhalation of 133-Xenon. *Circulation research* **20**: 124-135, 1967.

27. Park CS, Payne SJ. A generalized mathematical framework for estimating the residue function for arbitrary vascular networks. *Interface Focus* **3**: 20120078, 2013.

28. Park CS, Payne SJ. Modelling the effects of cerebral microvasculature morphology on oxygen transport. *Medical engineering & physics* **38**: 41-47, 2016.

29. Pries AR, Secomb TW. Microvascular blood viscosity in vivo and the endothelial surface layer. *American journal of physiology. Heart and circulatory physiology* **289**: H2657-2664, 2005.

30. Reichold J, Stampanoni M, Lena Keller A, Buck A, Jenny P, Weber B. Vascular graph model to simulate the cerebral blood flow in realistic vascular networks. *J Cereb Blood Flow Metab* **29**: 1429-1443, 2009.

31. Risser L, Plouraboue F, Cloetens P, Fonta C. A 3D-investigation shows that angiogenesis in primate cerebral cortex mainly occurs at capillary level. *International journal of developmental neuroscience : the official journal of the International Society for Developmental Neuroscience* **27**: 185-196, 2009.

32. Su SW, Catherall M, Payne S. The influence of network structure on the transport of blood in the human cerebral microvasculature. *Microcirculation* **19**: 175-187, 2012.

33. Wahle A, Wellnhofer E, Mugaragu I, Sauer HU, Oswald H, Fleck E. Quantitative volume analysis of coronary vessel systems by 3-D reconstruction from biplane angiograms. *Proc Med Imaging Conf (San Francisco)* **2**: 1217-1221, 1993.

34. Zweifach BW, Lipowsky HH. Quantitative studies of microcirculatory structure and function. III. Microvascular hemodynamics of cat mesentery and rabbit omentum. *Circulation research* **41**: 380-390, 1977.

TABLES

Table 1. Table of values chosen to model penetrating vessels.

Variable	Morphological Values	Model Values
Arteriole Diameter (μm)	15 – 240[a]	40
Venule Diameter (μm)	20 – 125[a]	110
Length (mm)	Up to 2.5[a]	1.25
Surface density (/mm^2)	8.44 – 15[b]	12
Penetrating Vessel Order	3 – 5[c]	4

[a] Duvernoy et al. [8] [b] Risser et al. [31] [c] Cassot et al. [3]

Table 2 Mean and standard deviation of computed variables of interest and their corresponding morphological measurements.

	Computed Model Values	Morphological Measurements
Arteriole Mean Vessel Density (/mm^3)	382.1 ± 68.7	385.1[a]
Venule Mean Vessel Density (/mm^3)	280.1 ± 42.5	281.2[a]
Length-to-Diameter Ratio	9.46 ± 8.42	10.37 ± 9.41[b]
A1/A0	1.06 ± 0.54	0.984 ± 0.46[a]
A2/A0	0.646 ± 0.45	0.642 ± 0.294[a]
A2/A1	0.614 ± 0.28	0.686 ± 0.213[a]
(A1+A2)/A0	1.70 ± 0.90	1.626 ± 0.684[a]
α_{01} (rads)	1.047 ± 0.20	1.109 ± 0.238[a]
α_{02} (rads)	0.942 ± 0.18	0.999 ± 0.227[a]
α_{12} (rads)	0.820 ± 0.223	0.906 ± 0.239[a]
Asymmetry (rads)	0.106± 0.291	0.111 ± 0.373[a]

[a] Cassot et al. (including supplementary material) [4]; [b] Lorthois et al. [21]

Table 3 Parameters calculated for the full vascular network (including capillary network) using 40 μm penetrating vessels and 25 μm penetrating vessels, as well as the equivalent morphological measurements.

Parameter	25 μm Penetrating Arteriole	40 μm Penetrating Arteriole	Morphological Measurements[a]
Total Length/mm^3 (mm/mm^3)	497.5 ± 12.2	527.4 ± 20.7	411.16 – 613.17
Vascular Surface/mm^3 (mm^2/mm^3)	11.5 ± 1.18	15.9 ± 3.28	10.19 – 12.85
Vascular Volume (% of total volume) – 2.5mm depth	2.15 ± 0.54	4.55 ± 2.6	2.39 – 3.02
Volume/Surface (μm)	3.41 ± 1.77	5.69 ± 2.95	2.1 – 2.4
Mean Segment Length (μm)	59.7 ± 9.4	65.7 ± 15.9	52.67 ± 50.38

[a] Lauwers et al. [18].

Table 4 The mean tree resistance (R_μ) and standard deviation of the tree resistance (R_σ) along with the CBF for each diameter of penetrating vessel. The CBF is calculated assuming a 2:1 ratio of arterioles to venules and 12 trees/mm^2 surface density.

Penetrating Diameter	25 μm (arteriole)	40 μm (arteriole)	110 μm (venule)
R_μ (kg m^{-4} s^{-1})	3.4846 x 10^{14}	4.2801 x 10^{13}	8.9092 x 10^{11}
R_σ (kg m^{-4} s^{-1})	7.899 x 10^{13}	8.6576 x 10^{12}	1.2307 x 10^{11}
Mean CBF (mL min^{-1} 100g^{-1})	0.58	4.60	46.0
σ CBF(%)	36	27	18
IQR CBF (%)	80 – 108	82 - 110	89 - 106

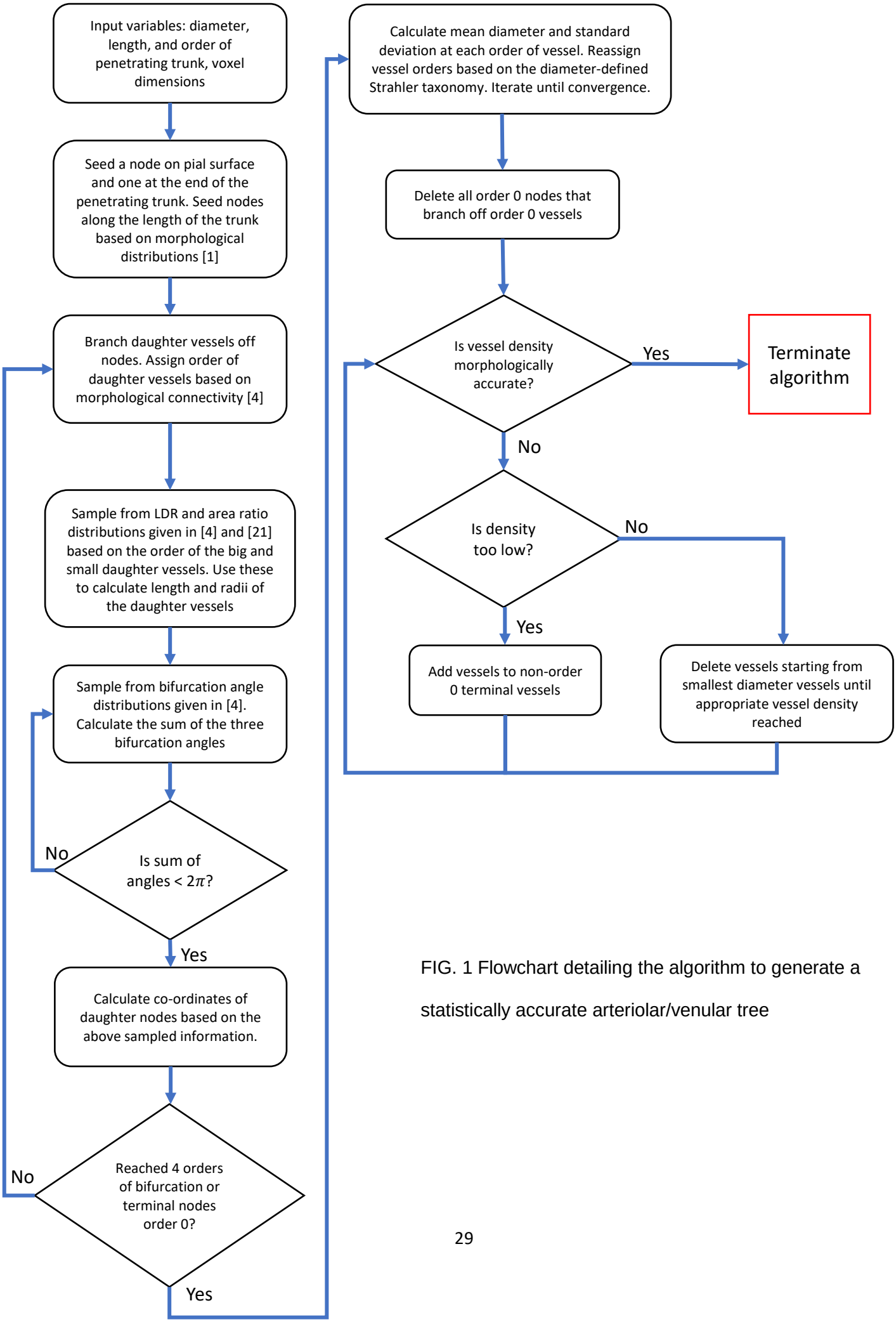

FIG. 1 Flowchart detailing the algorithm to generate a statistically accurate arteriolar/venular tree

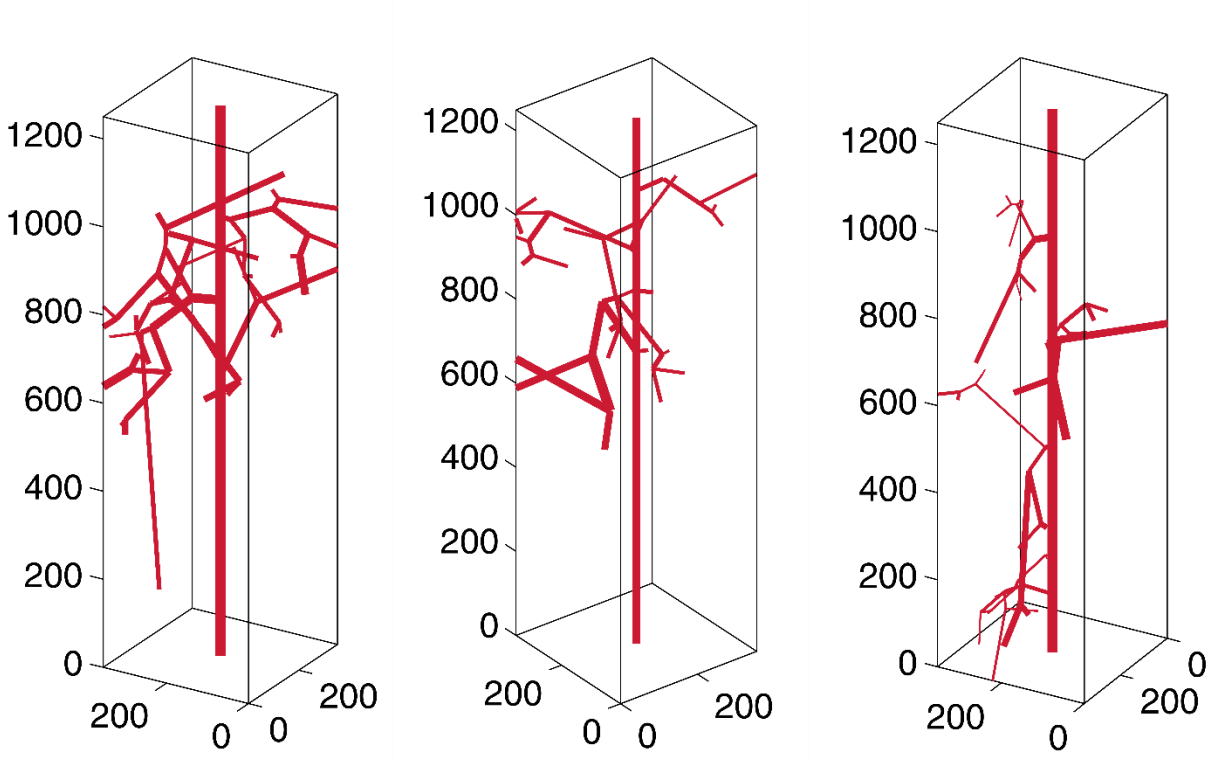

FIG. 2 Three examples of randomly generated morphologically accurate penetrating arterioles

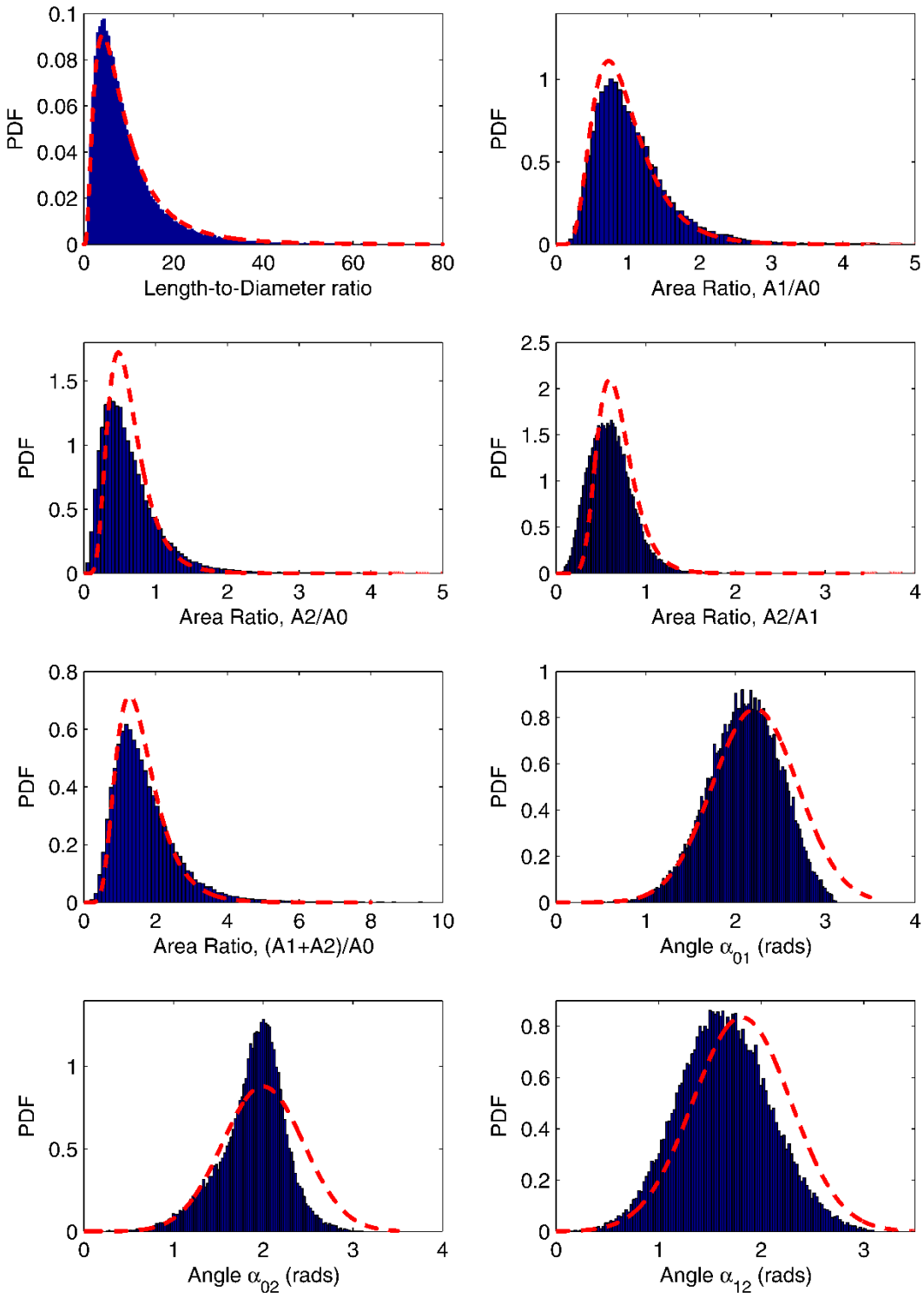

FIG. 3 Histograms of the simulation data (blue bars) generated using the algorithm, and the morphologically calculated distributions (red dotted line) taken from [4,21]

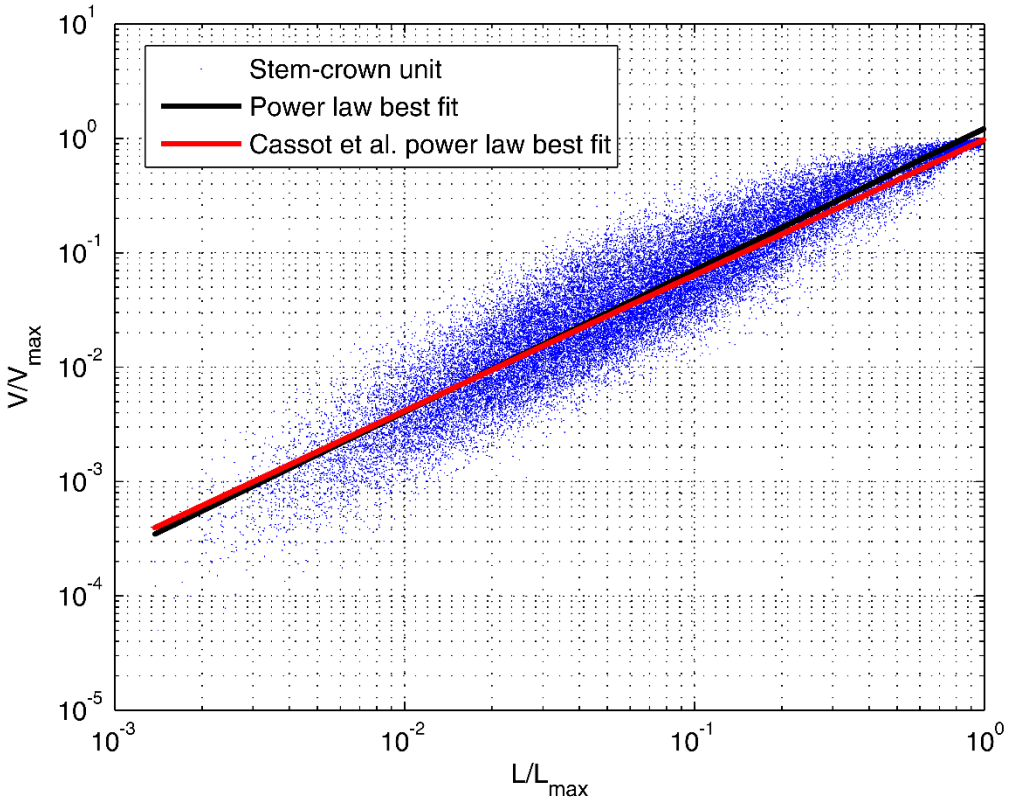

FIG. 4 Normalized cumulative volume-length relationships for all bifurcations simulated, along with power law fit (solid black line), and experimental fit (solid red line).

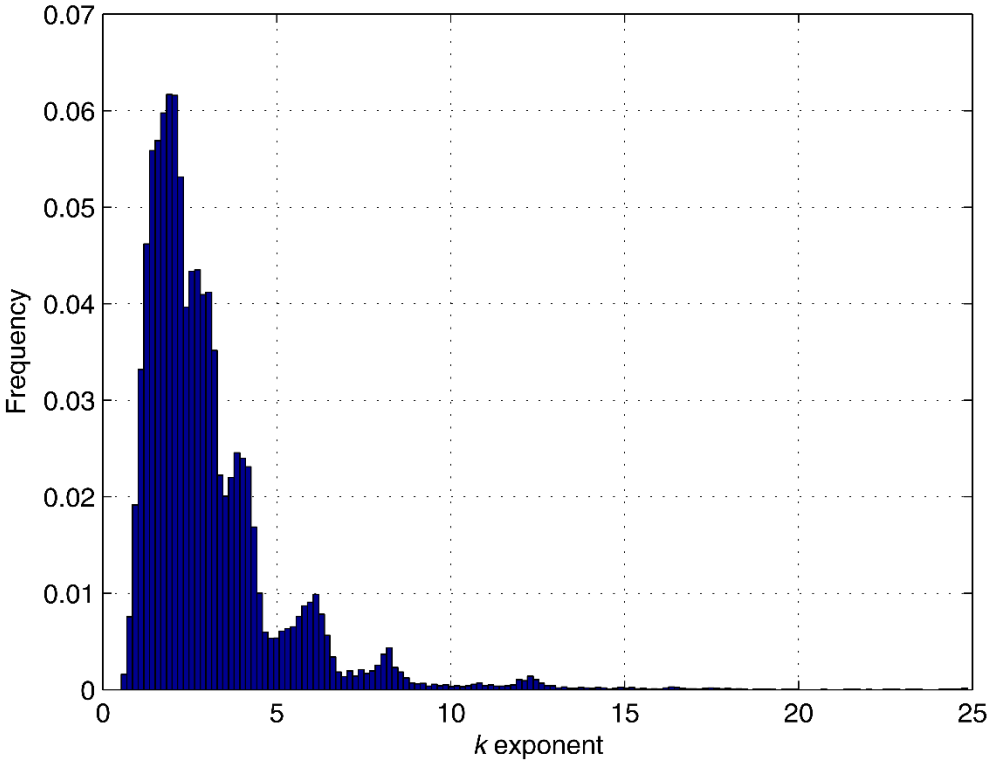

FIG. 5 Distribution of *k* exponent over all the bifurcations simulated by the algorithm